Low-temperature route to metal titanate perovskite nanoparticles for photocatalytic applications

Tarek Alammar [a], Ines Hamm [a,b], Michael Wark [b,c,*], Anja-Verena Mudring [a,d,**]

[a] Inorganic Chemistry III, Ruhr-University Bochum, Universitaetsstrasse 150, 44801 Bochum, Germany
[b] Laboratory for Industrial Chemistry, Ruhr-University Bochum, Universitaetsstrasse 150, 44801 Bochum, Germany
[c] Institute for Chemistry, Technical Chemistry, Carl von Ossietzky University Oldenburg, Carl-von-Ossietzky-Str. 9-11, 26129 Oldenburg, Germany
[d] Materials Science and Engineering, Iowa State University and Critical Materials Institute, Ames Laboratory, Ames, IA 50010, USA

ARTICLE INFO

ABSTRACT

$MTiO_3$ (M = Ca, Sr, Ba) nanoparticles were synthesized by a one-step room-temperature ultrasound synthesis in ionic liquid. The obtained samples are characterized by X-ray diffraction, scanning electron microscopy, nitrogen adsorption, UV–vis diffuse reflectance, Raman and IR spectroscopy and their capability in photocatalytic hydrogen evolution and methylene blue degradation was tested. Powder X-ray diffraction and Raman spectroscopic investigations revealed the products to crystallize in the cubic perovskite structure. SEM observations showed that the obtained $CaTiO_3$ consists of nanospheres, $BaTiO_3$ of raspberry-like shaped particles of 20 nm in diameter. $SrTiO_3$ particles have cubic-like morphology with an edge length varying from 100 to 300 nm. $SrTiO_3$ exhibited the highest catalytic activity for photocatalytic H_2 evolution using only 0.025 wt.% Rh as co-catalyst and for the degradation of methylene blue under UV irradiation. The influence of parameters such as synthesis method, calcination temperature, and doping with nitrogen on the morphology, crystallinity, chemical composition, and photocatalytic acivity of $SrTiO_3$ was studied. Heating the as-prepared $SrTiO_3$ to 700 °C for extended time leads to a decrease in surface area and catalytic activity. Ionothermal prepared $SrTiO_3$ exhibits a higher activity than sonochemically prepared one without co-catalyst due to a synergistic effect of anatase which is present in small amount as a by-phase. After photodeposition of Rh, however, the activity is lower than that of the sonochemically prepared $SrTiO_3$. Nitrogen-doped $SrTiO_3$ showed photocatalytic acivity under visible light irradiation.

1. Introduction

Photocatalytic water splitting to produce hydrogen is attracting tremendous attention owing to its potential as an alternative fuel source that places no burden on the environment [1]. Although many attempts have been devoted in recent years to prepare various kinds of photocatalysts to form hydrogen by water splitting the efficiency of the present materials is not high enough to be economically viable and suitable for use. Thus, enhancement of the water splitting efficiency but also simplification of the photocatalyst preparation is still important challenges.

Ternary perovskites $MTiO_3$ (M = Ca, Sr, Ba) are wide bandgap semiconductor materials with interesting electronic, optical, magnetic and catalytic properties. The family of titanates is regarded as promising photocatalysts because of its excellent resistance against photocorrosion, its high thermal stability and the high structure stability when doped with metal ions to alter the opto-electrical properties [2].

The typical method to prepare the $MTiO_3$ relies on the solid-state reaction of MCO_3 and TiO_2 at temperatures above 900 °C; quite often the obtained products contain agglomerated particles of different sizes and morphologies as well as impurities owing to incomplete reaction [3]. Therefore, exploring a new technique to prepare well-defined, size and shape controlled $MTiO_3$ by a cost effective reaction with environmentally benign reagents and mild and energy-efficient preparation conditions is desirable [4].

Recently, much attention has been devoted to the preparation of nano-structured inorganic materials with various morphologies, sizes, and dimensions by ultrasound synthesis and sonochemistry, which is considered as a green route [5]. The sonochemical process, basically operating near room temperature relies on acoustic

* Corresponding author at: Institute for Chemistry, Technical Chemistry, Carl von Ossietzky University Oldenburg, Carl-von-Ossietzky-Str. 9-11, 26129 Oldenburg, Germany. Tel.: +49 441 798 3675; fax: +49 441 798 3330.
** Corresponding author at: Department of Materials Science and Engineering, Iowa State University and Critical Materials Institute, Ames Laboratory, Ames, IA 50010, USA. Tel.: +1 515 294 1569; fax: +1 515 294 0999.
E-mail addresses: michael.wark@uni-oldenburg.de (M. Wark), mudring@iastate.edu (A.-V. Mudring).

cavitation. In a liquid subjected to ultrasound waves extremely high temperatures of up to 5000 K and pressures of 800 atm can be locally achieved for very short times [4]. These conditions are sufficient to induce either chemical or physical transformations under seemingly mild conditions. For that reason, sonochemistry typically is considered to be a green synthesis method and represents an alternative to the conventional high temperature synthesis route but also to hydrothermal, solvothermal, sol–gel, co-precipitation, electrochemical deposition, pyrolysis and other techniques which typically require thermal post-treatment of the samples for full conversion to the ternary oxide. In addition, most of the latter named synthetic methods involve air and temperature sensitive organometallic precursors or environmentally critical agents [6].

Room-temperature ionic liquid (RTILS) emerged in recent years as reaction media for nanomaterial synthesis. Their self-organization and micro phase-separated structure renders them as a templating agent, whereas their amphiphilic nature can be employed in the stabilization of the resultant nanoparticles [7,8]. The use of ionic liquids as a reaction medium in sonochemistry is advantageous because of their low measurable vapor pressure, low viscosity, low thermal conductivity, and high chemical stability, which are all important parameters to generate efficient cavitation. In this work, we employed sonochemistry for the synthesis of nano-$MTiO_3$ (M = Sr, Ba, Ca) in ionic liquid; the latter acting as a solvent and also as a structure-directing agent. The effects of variation of the preparation method, calcination temperature and doping with nitrogen on the morphology, size, and the catalytic activity toward methyl blue degradation as well as photogeneration of H_2 were investigated in detail for $SrTiO_3$.

2. Experimental

2.1. Materials

All reagents employed were commercially available and directly used without further purification. The ionic liquid 1-butyl-3-methylimidazolium bis-(trifluoromethanesulfonyl)imide, $[C_4mim][Tf_2N]$, was prepared according to modified common procedures reported in the literature [9]. We used: lithium bis(trifluoromethansulfonyl)imide (99%) from Iolitec, 1-methylimidazole (99%), ethanol (p.a.), 1-chlorobutane (99%) and titanium (IV) isopropoxide (97%) from Sigma–Aldrich, sodium hydroxide (98%), acetonitrile (99.5%), ethylacetate (99%) from J.T. Baker, strontium acetate hydrate (99%), calcium acetate hydrate (99%) from ABCR and barium acetate (99%) from Fluka.

2.2. Synthesis of $MTiO_3$ (M = Sr, Ba, Ca)

A series of samples were prepared by adding stoichiometric amounts of $M(CH_3COO)_2 \cdot xH_2O$ (M = Sr, Ba, Ca), $Ti(OiPr)_4$ (OiPr = isopropoxide) and 1.5 g finely ground NaOH powder to a mixture of 1 mL deionized water and 2 mL ionic liquid. The reaction mixture was stirred vigorously for 30 min, and then irradiated with ultrasound (USC200T, VWR International; 45 kHz, 60 W) in a glass tube sealed with a screw cap under ambient conditions for 10 h. The product was separated by centrifugation, washed thoroughly with ethanol and distilled water and dried overnight in air at 80 °C. To enhance the crystallinity of $CaTiO_3$, the dried $CaTiO_3$ was calcined in air at 700 °C for 5 h.

Ionothermal synthesis experiments were performed with the mixtures described above in 50 ml Teflon© cups enclosed in stainless steel autoclaves (Parr Instruments) into a laboratory furnace which was held at 170 °C for 20 h. At that time, the autoclave was cooled in air to room temperature. The resulting powders were separated by centrifugation, washed with ethanol and deionized water several times, and finally dried in the oven at 80 °C overnight.

To prepare nitrogen-doped $SrTiO_3$ samples, the sonochemically prepared $SrTiO_3$ powder (where $[C_4mim][Tf_2N]$ was used as the solvent) was mixed with urea and calcined at 450 °C for 2 h. The weight ratio of urea to $SrTiO_3$ corresponded to 1:2.

2.3. Characterization

2.3.1. Powder diffraction
Powder X-ray diffraction measurements were carried out on a G670 diffractometer with an image plate detector (Huber, Rimsting, D) operating with MoK_α radiation ($\lambda = 0.07107$ nm).

2.3.2. Scanning electron microscopy (SEM)
Scanning electron microscopy measurements were performed with a high resolution SEM (Zeiss, LEO 1530 Gemini) with a field emission gun (FEG) and an acceleration voltage of $U_{acc} = 0.2–30$ kV. For the SEM measurements the $MTiO_3$ nanopowders were put on a carbon-film, dried under vacuum for 20 min and covered with gold to allow for a better electronic conductivity.

2.3.3. IR spectroscopy
Attenuated total reflection (ATR) spectroscopy was carried out on an Alpha ATR spectrometer equipped with a diamond crystal (Bruker, Karlsruhe, D). Solid samples were pressed on the crystal.

2.3.4. Raman spectroscopy
Raman spectra were obtained at 150 mW on a Bruker IFS-FRA-106/s at room temperature.

2.3.5. UV–vis spectroscopy
UV–vis spectra were measured at room temperature on a Cary 5000 spectrometer (Varian) in diffuse reflection mode.

2.3.6. Nitrogen physisorption
Nitrogen physisorption experiments were carried out in modified Autosorb 1C setup (Quantachrome). The samples were thermally pretreated at 200 °C for 2 h in He. The physisorption measurement was performed at the boiling point of liquid N_2 (78 K). The surface area is calculated according to the BET (Brunauer–Emmett–Teller) equation. The pore size distribution was obtained by the BJH (Barrett–Joyner–Halenda) method.

2.3.7. Photocatalytic activity tests
2.3.7.1. Hydrogen generation. Photocatalytic hydrogen generation from methanolic solutions was carried out in a closed gas system using a double-walled inner irradiation-type quartz reactor, which contained a suspension of 500 mg photocatalyst in 540 ml water and 60 ml methanol (0.83 g/l). For irradiation a 700 W Hg immersion lamp (set to 57% power = 400 W) was used; by actinometry a photon flux of about 6.4×10^{-5} mol photons/s was determined. Hydrogen evolution was detected online using a multi-channel analyzer (Emerson) equipped with a detector for the determination of the concentration of hydrogen (paramagnetic detector). Argon was used as the carrier gas. The continuous gas flow (50 NmL/min) was controlled by a Brockhorst mass flow controller. All reactions were performed at 286 K. The whole system was flushed with nitrogen at 100 NmL/min to remove any trace of air prior irradiation. The co-catalyst Rh (0.5 wt.%) was deposited onto the photocatalyst via reductive photodeposition from Na_3RhCl_6 solution [10]. The N-doped sample was measured with the continuous gas flow of 25 N mL/min using the double-walled inner irradiation-type quartz reactor filled with a 2 M $NaNO_2$ solution to cut-off the UV light. $NaNO_2$ solution is a known cut-off solution to block the UV light (Fig. SI-1). It has been used in several photocatalytic studies, e.g.

[11], and is recommended as a calibration standard for photospectrometers by Hellma Analytics.

2.3.7.2. Photodegradation of methylene blue.

The catalytic test was carried out in a reactor, which contained a suspension of 100 mg photocatalyst in 100 mL (1.0 g/l) water containing 10 ppm methylene blue. The suspension was continuously stirred in the dark for 30 min to accomplish adsorption/desorption equilibrium, and then illuminated using a 290 W Xe arc lamp (Newport Oriel Instruments). The lamp was switched on 30 min prior to the illumination of the samples in order to stabilize the power of its emission at $\lambda > 320$ nm (a cut-off filter FSQ-WG320 was used to remove light with wavelengths below 320 nm). Every 30 min about 3 mL aliquots were sampled and filtered by nylon syringe filters (pore size 0.2 μm) to remove the photocatalyst before analysis by UV–vis spectrophotometer (Varian Cary 50) at 664 nm corresponding to the maximum absorption wavelength of MB.

3. Results and discussion

3.1. Characterization of titanates from sonochemical syntheses

1-Butyl-3-methylimidazolium bis(trifluoromethanesulfonyl) imide, [C$_4$mim][Tf$_2$N], was used in this study as it is one of the most common room temperature ionic liquids with an appreciably low viscosity, high thermal, chemical and redox stability. The [Tf$_2$N]$^-$ anion is known to be weakly coordinating and has a comparatively small direct impact on the phase, size and morphology of the reaction products when compared to the cation [C$_4$mim]$^+$. [C$_4$mim]$^+$ (Fig. SI-2) is based on a short-chain alkyl methylimidazolium cation and has a high electron acceptor potential due to the delocalized aromatic system which is highly likely to create electrostatic attractions on the surface of oxide particles. Due to the electron deficit in the C=N bond the C2-H bond is highly polarized and the associated proton has the strongest acidity [12,13]. Thus, H-bond-like interactions may also occur as a result of the acidic character of the imidazolium ring-bound hydrogen atoms [14]. It is believed that both electrostatic and coordinative effects of imidazolium cations contribute to nanoparticle stabilization in such ionic liquids. The low interface energies of ionic liquids lead to good stabilization. Furthermore, the low interface tension of ionic liquid leads to high nucleation rates and a very weak Ostwald ripening, favorable for the formation of very small nanoparticles [15].

To characterize the phase purity and crystallinity of the obtained material, XRD patterns for all samples were measured. Fig. 1 presents the XRD patterns of sonochemically prepared MTiO$_3$ in [C$_4$mim][Tf$_2$N]. All of the diffraction peaks can be indexed to the cubic perovskite structure of CaTiO$_3$ (75–2100), SrTiO$_3$ (35–734), and BaTiO$_3$ (PDF 31–174). No impurity peaks such as those of TiO$_2$ or MO or evidence for other MTiO$_3$ polymorphs can be detected. For BaTiO$_3$ five crystalline forms are known, of which three are ferroelectric (rhombohedral, orthorhombic, tetragonal) and stable below 120 °C. The cubic form is stable above 120 °C up to 1460 °C; beyond this temperature a hexagonal structure is formed [16]. The CaTiO$_3$ faces a transition from the room temperature stable orthorhombic structure to a tetragonal polymorph between 1100 and 1150 °C followed by a transformation to the cubic structure type at 1250 °C [17]. Furthermore, the SrTiO$_3$ endures a cubic to tetragonal transition on cooling at $T = 105$ K (-168.15 °C) [18]. Thus, only for SrTiO$_3$ the cubic aristotype is the thermodynamically stable form at room temperature. Quite astonishingly under the chosen synthesis conditions also for CaTiO$_3$ and BaTiO$_3$ the cubic aristotype was obtained, seemingly at room temperature. The reason why the high temperature forms are obtained seems to result from the unusual reaction conditions: Under ultrasound irradiation, for a short time and at the point of phase formation high temperatures and high pressures are present resulting in the formation of the corresponding phase. The cubic phases are also favored by high pressures; as the pressure and temperature drop quite fast, no phase transformation occurs.

The crystal domain sizes (D_{hkl}) have been estimated from the most intense diffraction peak (1 1 0) according to the Scherrer equation. The crystallite sizes vary from 8.8 nm to 16 nm (Table 1). Relative crystallinity was estimated by the comparison of the XRD peak area ratios of the as-prepared MTiO$_3$ (Sr, Ba) and calcined CaTiO$_3$ (1 1 0) peaks with the (1 1 0) peak of well-crystalline rutile-type TiO$_2$ after mixing 67% of MTiO$_3$ and 33 wt.% of rutile (Fig. SI-3). The peak area ratios range from 1.76 to 3.16 as listed in Table 1. Among all samples, BaTiO$_3$ shows the relatively best crystallinity and the largest crystal particle size of 16 nm, whereas the CaTiO$_3$ is the least crystalline material even after calcination, and exhibits the smallest crystallite size of 8.8 nm.
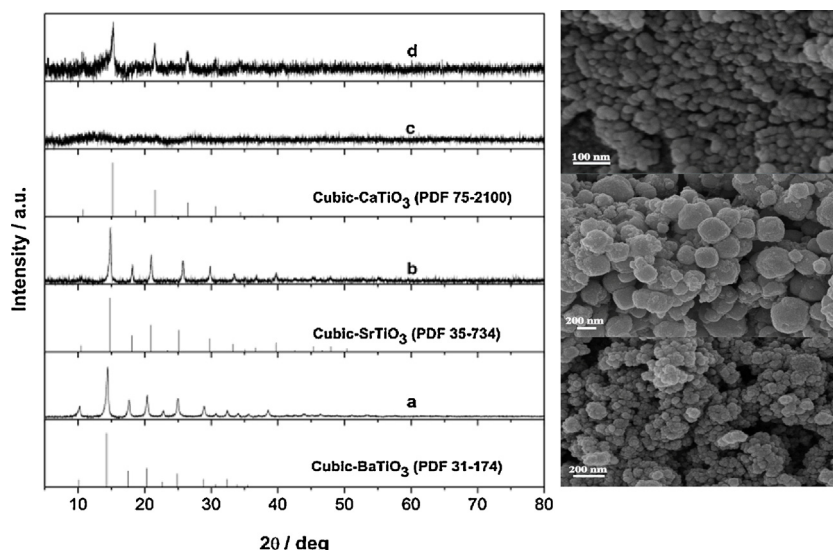

Fig. 1. XRD patterns of as-prepared SrTiO$_3$ (a), BaTiO$_3$ (b), CaTiO$_3$ (c), and calcined CaTiO$_3$ (d) in comparison with the database patterns, and SEM images of calcined CaTiO$_3$ (top, right), SrTiO$_3$ (middle, right), and BaTiO$_3$ (bottom, right).

Table 1
Estimated crystal sizes using Scherrer equation, relative crystallinity, band gaps from Tauc plots resulting from diffuse reflectance UV–vis spectra, and texture properties of as-prepared $SrTiO_3$, $BaTiO_3$, and calcined $CaTiO_3$.

Sample	Crystallite size [nm]	XRD peak ratio[a]	Band gap [eV]	BET surface area, S_{BET} [m² g⁻¹]	Nitrogen pore volume, V_{pore} [cm³ g⁻¹]	Pore diameter [nm]
$CaTiO_3$	8.8 ± 0.2	1.76	3.2	147.29	0.48	7
$SrTiO_3$	14.2 ± 0.2	2.43	3.1	47.08	0.07	1.9
$BaTiO_3$	16.0 ± 0.2	3.16	3.0	76.92	0.16	1.8

[a] XRD peak area ratio of the $MTiO_3$ (1 1 0) peaks and the rutile (1 1 0) peak.

The morphology of the samples was investigated by SEM, representative images are shown in Fig. 1. $CaTiO_3$ and $BaTiO_3$ particles are of almost regular spherical shape with a narrow and uniform particle size of about 20 nm. The primary spherical-like $SrTiO_3$ particles were found to agglomerate more strongly leading to cubic-like aggregates with edge lengths varying from 100 to 300 nm. Fig. 2 shows the Raman spectra of the as-prepared $SrTiO_3$, $BaTiO_3$, and calcined $CaTiO_3$ nanoparticles. The Raman spectrum of calcined $CaTiO_3$ does not exhibit any bands, indicating a disordered structure [19]. Based on the selection rules no first-order Raman active vibration frequencies are allowed for cubic $MTiO_3$ [20]. However, in the Raman spectra of as-prepared $MTiO_3$ (Sr, Ba) five bands can be observed at 179, 305, 517, 715, and 806 cm⁻¹. Such modes appear, however, when crystal symmetry breaking occurs [21]. The band observed at 806 cm⁻¹ may be attributed to the LO (longitudinal-optic) vibrational mode, with A_1 symmetry of the $[TiO_6]$ octahedron. The band at 715 cm⁻¹ is assigned to a transverse mode coupling related to the cubic phase of the titanate. The bands at 179 cm⁻¹ (TO_2) and 517 cm⁻¹ (TO_4) are assigned to polar transverse optic modes, where the band at 305 cm⁻¹ (TO_3) correspond to nonpolar modes [22].

Fig. SI-4 shows IR spectra of the as-prepared $SrTiO_3$, $BaTiO_3$, and calcined $CaTiO_3$ nanoparticles. The bands at 540 cm⁻¹ can be attributed to the Ti–O stretching mode [23]. No bands from ionic liquid or other impurities can be observed.

The optical absorption of the as-prepared $SrTiO_3$ and $BaTiO_3$, as well as the calcined $CaTiO_3$ was measured by UV–vis spectroscopy in diffuse reflectance. Fig. SI-5(left) shows the UV–vis spectra of the as-obtained $MTiO_3$ (Sr, Ba), and calcined $CaTiO_3$. The absorption spectra of the $MTiO_3$ samples exhibit onsets at 357 nm for $CaTiO_3$, 382 nm for $SrTiO_3$ and 388 nm for $BaTiO_3$, respectively, which are consistent with charge transfer from the valence band (mainly made of O 2p states) to the conduction band (mainly composed of Ti 3d states). The onset absorption values are determined by the linear extrapolating of the steep part of the UV absorption toward the base line.

The optical band gap (E_g) of the samples can be calculated on the basis of the optical absorption spectra by the following equation (Tauc plot):

$$(\alpha h\nu)^n = B(h\nu - E_g)$$

where $h\nu$ is the photon energy, A is the absorbance, B is the related to the effective masses associated with the valence and conduction bands and n is either $n = 2$ for an indirect allowed transition or $n = 1/2$ for the direct forbidden transition. Plotting $(\alpha h\nu)^{1/2}$ versus $h\nu$ based on the spectral response gives the extrapolated corresponding E_g values [10,24]. As shown in Fig. SI-5 (right) when M^{2+} changes from Ba^{2+} to Sr^{2+} and then to Ca^{2+}, with the decreasing ionic radius, the band gaps of $MTiO_3$ are varying from 3.0 to 3.2 eV, respectively (Table 1). Table SI-1 shows a comparative between the band gap values of $MTiO_3$ (Ca, Sr, Ba) obtained in this work with representative values reported in the literature. As can be seen in this table, the estimated band gaps of all sonochemically prepared $MTiO_3$ are slightly (0.05–0.3 eV) lower than those reported in previous studies, but the same trend is observed when going from Ca to Ba. The lower band gap might have a positive impact on the photocatalytic activity with the sonochemically prepared $MTiO_3$ photocatalysts being theoretically slightly more efficient in light absorption.

The nitrogen adsorption–desorption isotherms and the corresponding pore size distributions of the synthesized samples are shown in Fig. 3 and Fig. SI-7, respectively; their texture properties are listed in Table 1. The isotherms of the synthesized samples are of type IV and are characteristic of mesoporous materials, according to the IUPAC classification; whereas the mesoporosity results from voids between the particles. The largest pore volume of 0.48 cm³ g⁻¹ was observed for $CaTiO_3$, the sample with the lowest crystallinity. The pore sizes of as-prepared samples are varied from
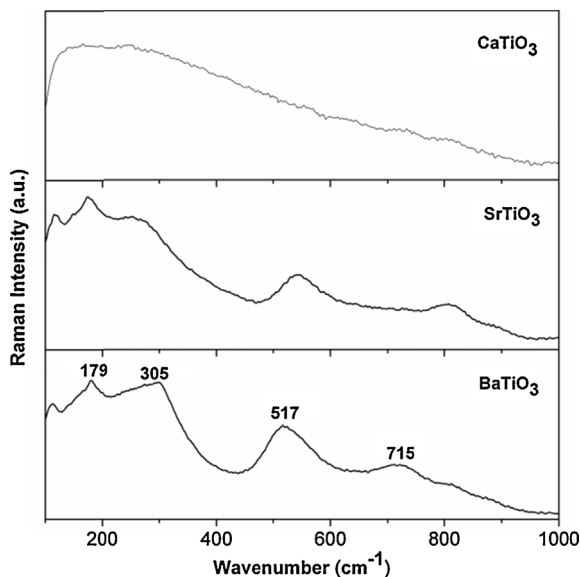

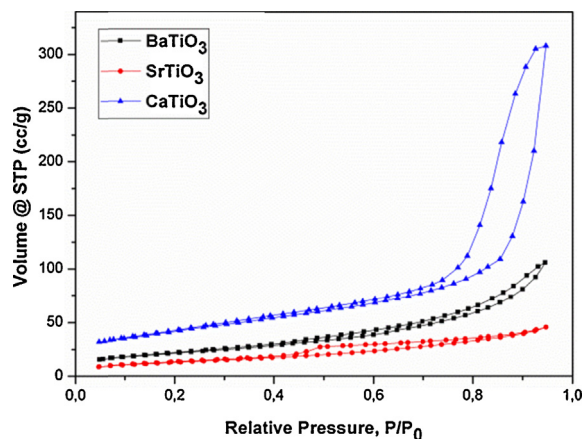**Fig. 2.** Raman spectra of as-prepared $SrTiO_3$, $BaTiO_3$, and calcined $CaTiO_3$.

Fig. 3. N₂ adsorption–desorption isotherms of as-prepared $SrTiO_3$, $BaTiO_3$, and calcined $CaTiO_3$.
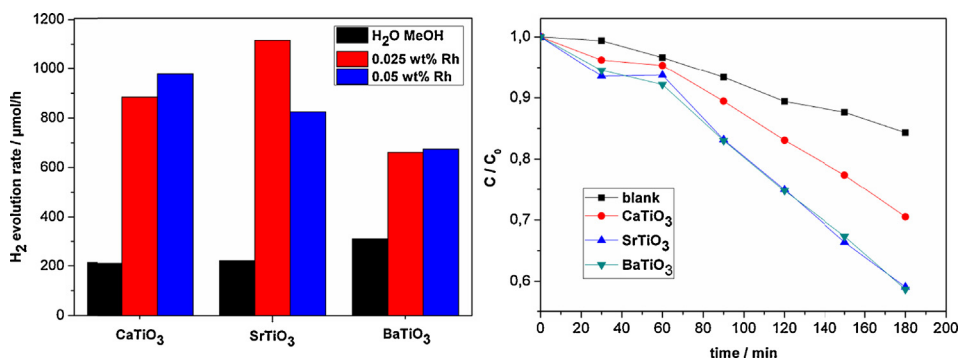
Fig. 4. Concentration changes of methylene blue dye as a function of irradiation time during the degradation process (right), and hydrogen production rate from solutions containing 10 vol.% methanol in water over MTiO$_3$ (M = Ca, Sr, Ba) and after photodeposition of Rh as co-catalyst (left).

1.8 nm for BaTiO$_3$ to 1.9 nm for SrTiO$_3$ with relatively narrow pore size distribution to 7 nm for CaTiO$_3$ with wide pore size distribution determined by the BHJ method from the adsorption branch of the isotherms. It is well known that the shape of the hysteresis loop in the adsorption/desorption isotherms gives information about the nature of the pores, where each type of adsorption isotherm is associated with a characteristic type of pore. The curves of as-prepared SrTiO$_3$ and to a lower extent also of the BaTiO$_3$ show a triangular shape and a steep desorption branches which can be ascribed to a pore connectivity effect resulting from the presence of pores with narrow mouths (ink-bottle pores). It is proposed that these pores might result from the presence of the ionic liquid in the synthesis. The shape of the isotherm of calcined CaTiO$_3$, however, indicates the presence of slit-shaped mesopores and interconnected pores with bottleneck shape, respectively. Moreover, high surface areas are obtained as listed in Table 1 and the specific surface areas vary from 47.1 m^2 g^{-1} for as-prepared SrTiO$_3$ to 147.3 m^2 g^{-1} for calcined CaTiO$_3$.

The as-prepared SrTiO$_3$ sample shows very high surface area which is significantly larger than that for bulk SrTiO$_3$ (1.78 m^2 g^{-1}) as well those of previously reported SrTiO$_3$ synthesized by sol–gel process using a solvent mix of ethylene glycol acting as stabilizer and H$_2$O (9 m^2 g^{-1}) [25], or mesoporous-assembled SrTiO$_3$ nanocrystal prepared by using ethanol, and ethylene glycol as a solvent, while cetyltrimethylammoniumchloride was used as a structure-directing surfactant (16.4 m^2 g^{-1}) [26], but still lower than this of SrTiO$_3$ nanoparticles prepared via a modified polymeric precursor method (80 m^2 g^{-1}) [27]. The BET value of as-prepared BaTiO$_3$ is larger than that reported for nanosized BaTiO$_3$ powder prepared by precipitation of a titanium ester with Ba(OH)$_2$ (60 m^2 g^{-1}) [28]. However, high surface area (301 m^2 g^{-1}) is also reported for CaTiO$_3$ formed from CaO and TiO$_2$ at 1000 °C for 20 h, but only after additional mechanochemical treatment [29].

3.2. Photocatalytic activities of titanates from sonochemical syntheses

3.2.1. Photodegradation of methylene blue

Photocatalytic activities of the three samples were first evaluated by the degradation of methylene blue (MB) under UV irradiation. When a photocatalyst absorbs photons with energies larger than the band gap, electrons are promoted from the valence band to the conduction band, leaving holes behind in the valence band. Both electrons and holes either migrate to the surface of the particles or might endure an undesired recombination. The holes react with absorbed water molecules generating OH radicals, which are responsible for the photocatalytic heterogeneous degradation of methylene blue [30].

Fig. 4 (right) displays the concentration changes of MB as a function of the irradiation time. The blank experiment without adding any photocatalyst indicated that the photolysis rate of MB is not negligible, but clearly slower than the degradation over MTiO$_3$ (M = Ca, Sr, Ba). The activities of MTiO$_3$ (M = Ca, Sr, Ba) and P25 follow the order of P25 > BaTiO$_3$ = SrTiO$_3$ > calcined CaTiO$_3$. Kinetic studies indicate that the photocatalytic process follows a pseudo-first-order kinetic for MTiO$_3$ (M = Ca, Sr, Ba) and first-order kinetic for P25, ln(C_0/C_t) = kt, where C_0 is the initial MB concentration before irradiation, C is the concentration of MB after a specific UV irradiation time t, k is the rate constant for the reaction, which is estimated to be 0.014 min^{-1} (R = 0.981) for P25, 0.003 min^{-1} (R = 0.977) for MTiO$_3$ (Sr, Ba), and 0.0019 min^{-1} (R = 0.976) for calcined CaTiO$_3$. CaTiO$_3$ nanoparticles show the lowest performance for MB degradation although this sample exhibits the highest surface area, indicating that crystallinity is more important than porosity. It is very hard to compare the results with literature data. Xian et al. investigated the photocatalytic activity of synthesized SrTiO$_3$ using polyacrylamide gel method by degradation of various dyes including Congo Red (CR), Rhodamine B (RhB), methyl orange (MO), and methylene blue (MB) under irradiation with a 20 W low-pressure mercury lamp (λ = 365 nm) for 10 h. It was observed that the degradation percentage is dependent on the type of dye, where CR showed the highest activity of 85% and MB exhibited a degradation efficiency of 45% and followed the pseudo-first-order kinetic [31]. The sonochemically prepared SrTiO$_3$ in this study reached this percentage after only 3 h, but with a Xe lamp of higher power. For spherical CaTiO$_3$ Zhao et al. determined a degradation of ~30% after 10 min time with a rate of 0.045 min^{-1}. The shown curves indicate a pseudo-first-order kinetic, however they give no information on the power and the kind of the lamp they used [32]. Lin et al. [33] determined a degradation efficiency of 7% after 50 min and a rate of degradation of 0.0016 min^{-1} (R = 0.989) following pseudo-first-kinetics for BaTiO$_3$, prepared by a high temperature solid-state reaction between BaCO$_3$ and TiO$_2$, in photobleaching of MB aqueous solution under irradiation with 500 W high pressure mercury lamp (λ = 365 nm). The sonochemically prepared BaTiO$_3$ showed a comparable efficiency but with a Xe lamp of less power.

3.2.2. Hydrogen generation

The photocatalytic properties of MTiO$_3$ (M = Ca, Sr, Ba) and P25 for H$_2$ evolution from water were tested using 10% methanol aqueous solution as the sacrificial agent under UV light irradiation. As shown in Fig. 4, without any co-catalysts the H$_2$ evolution rates of MTiO$_3$ (M = Ca, Sr, Ba) are already as high as 214 ± 8 μmol/h for calcined CaTiO$_3$, 225 ± 12 μmol/h for as-prepared SrTiO$_3$, 313 ± 10 μmol/h for as-prepared BaTiO$_3$, and 317 ± 5 μmol/h for
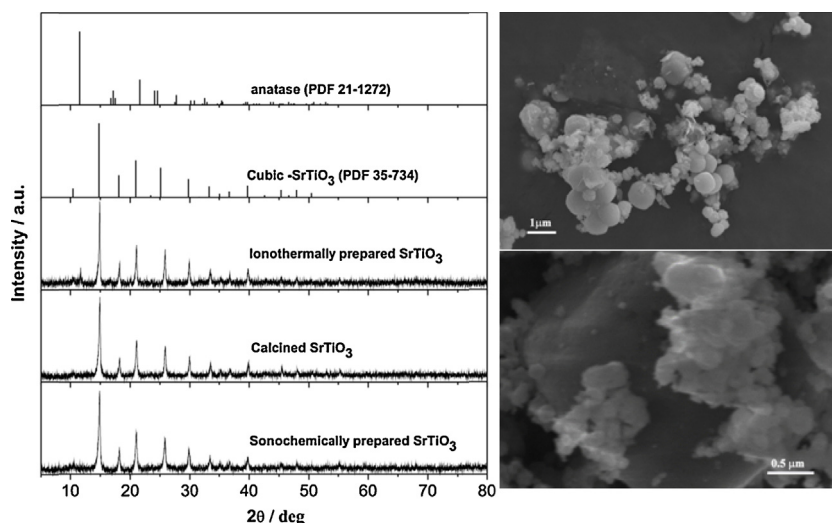
Fig. 5. (left) X-ray diffraction patterns of sonochemically prepared $SrTiO_3$ and its thermally treated sample at 700 °C for 5 h and ionothermally prepared $SrTiO_3$ in comparison with the database patterns, (right) SEM images of calcined $SrTiO_3$ (right-bottom) and ionothermally prepared $SrTiO_3$ (right-top).

P25, respectively, demonstrating that active surface sites for hydrogen generation are readily available on the catalyst surface. After loading with only 0.025 wt.% Rh by photodeposition, in which Rh is directly deposited on the titanates at the centers where reactive photogenerated electrons are available, the H_2 evolution rates of $MTiO_3$ (M = Ca, Sr, Ba) were increased to 886 ± 20 µmol/h for $CaTiO_3$, 1115 ± 25 µmol/h for $SrTiO_3$, 662 ± 18 µmol/h for $BaTiO_3$, and 950 ± 20 µmol/h for P25, since the charge carrier separation is improved. Addition of further Rh leads only to a minor additional increase in H_2 evolution for all four samples demonstrating that the deposited Rh nanoparticles should stay very small. $BaTiO_3$ exhibits the most active surface sites for hydrogen evolution and its activity is competitive to commercially available P25; however, the activity increases less with deposition of Rh, indicating that possibly larger Rh nanoparticles, being less active and absorbing more light by their own, shading the photocatalyst, are formed at the quite active surface sites. In all cases, however, the Rh deposited particles were too small to be doubtless observed by our transmission electron microscopy; thus, we conclude that their diameters are below 2 nm. In case of $SrTiO_3$ the lower activity of the hydrogen generating sites in the absence of Rh seems to help to limit the size of the photodeposited Rh particles.

Very often an increased surface area results in a better photocatalytic activity [34], because it affords more active sites, but it can also concomitantly increase the number of trap states that act as recombination sites [35]. The differences in photocatalytic activity between $BaTiO_3$ and $SrTiO_3$ compared to $CaTiO_3$ may arise predominantly from the higher crystallinity of the $BaTiO_3$ and $SrTiO_3$. The charge separation and migration of photogenerated carriers are strongly affected by the crystallinity of photocatalyst material. A higher crystallinity leads to a decreased amount of defects. Defects are known to serve as trapping and recombination centers between photogenerated carriers and thus, diminishing the photocatalytic behavior of a material [36].

3.3. Effect of calcination temperature

To evaluate the effect of heat treatment on phase, particle size and photocatalytic activity of the best sample, sonochemically prepared $SrTiO_3$, was calcined at 700 °C. From the XRD patterns for the as-prepared $SrTiO_3$ and its thermally treated sample (Fig. 5), no noticeable phase changes can be observed and all of the diffraction peaks match the cubic reference crystal structure of $SrTiO_3$

(PDF 35–734). However, the as estimated from the Scherrer equation increased from 14 ± 0.2 nm to about 17 ± 0.2 nm after heat treatment. The specific surface area of $SrTiO_3$ decreased from 47.1 m^2 g^{-1} to 38 m^2 g^{-1} after heat treatment at 700 °C (Fig. SI-8), which is due to some particle sintering.

Fig. 6 shows the photocatalytic activities over the as-prepared $SrTiO_3$ compared to its thermally treated sample. It can be seen that, as a result of calcination, the H_2 evolution rate of $SrTiO_3$ samples without any co-catalysts decreased from 225 ± 12 µmol/h to 65 ± 10 µmol/h and after loading 0.025 wt.% Rh from 1115 ± 25 µmol/h to 458 ± 20 µmol/h. Presumably, the thermal treatment causes particle sintering, resulting in a lower dispersion and reduction of accessible active sites. Bui et al. determined an activity of only 4.13 µmol H_2 after 2 h UV-irradiation of $SrTiO_3$ synthesized via a sol–gel route calcined at 900 °C (300 W Hg-lamp) [37]. $SrTiO_3$ nanocrystals, which were prepared via the sol–gel process with the aid of a structure-directing surfactant at 700 °C, exhibited a hydrogen production rate of 276 µmol/h from 50 vol.% methanol aqueous solution after loading 0.5 wt.% Pt (176 W Hg-lamp) [38]. Although such evolution rates are hard to compare in detail due to differences in the illumination, this rough comparison demonstrates that our new sonochemical synthesis route,
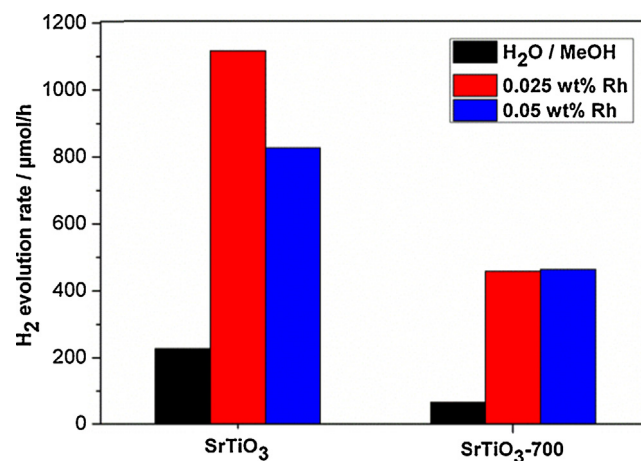

Fig. 6. Hydrogen production rate from solutions containing 10 vol.% methanol in water over as-prepared $SrTiO_3$ and its thermally treated sample, and after photodeposition of Rh as co-catalyst.
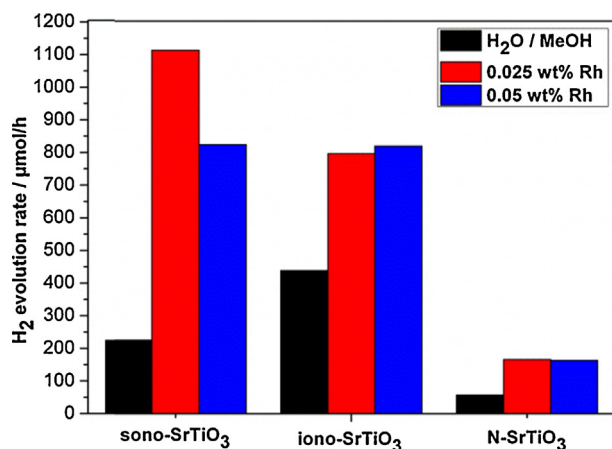
Fig. 7. Hydrogen production rate from solutions containing 10 vol.% methanol in water over sonochemically, ionothermally prepared $SrTiO_3$ and N–$SrTiO_3$ before and after photodeposition of Rh as co-catalyst.

Fig. 8. XRD patterns of as-prepared $SrTiO_3$, and N–$SrTiO_3$, the comparison of the position of (1 1 0) and (1 1 1) peaks shows shift due to nitrogen doping.

operating very energy-efficient at low temperatures, leads to very active titanate materials.

3.4. Effect of preparation method

In order to investigate the effect of the preparation method on the morphology, crystallization, and photocatalytic activity of $SrTiO_3$ classical heat conversion (also termed the ionothermal process) [39] was used instead of the sonochemical preparation method. All other reaction conditions were kept the same. During sonication of a liquid ultrasonic waves cause high and low-pressure regions: The low-pressure stage is associated with the formation and growth of microscopic bubbles. Collapse of these bubbles leads hot spots of extremely high temperatures and pressure [40]. The fast changing local conditions lead to high nucleation rates, but leave little time for crystallization and particle processes. In the ionothermal process indirect heating occurs through heat transfer from outside to the reaction medium which is associated with a slower heating rate, typically reducing the nucleation rate but promoting a higher crystallinity [41].

As shown in Fig. 5, the XRD pattern of the sample obtained using ionothermal process shows in addition to diffraction peaks originating from $SrTiO_3$ also diffraction peaks can be indexed to anatase. The crystal domain size of the ionothermally prepared sample has been estimated using Scherrer equation to be 18.5 ± 0.2 nm. This result confirms, as anticipated, that the sonochemical-assisted reaction conditions led to smaller particles compared to the ionothermal method. SEM image of ionothermal prepared $SrTiO_3$ shows the formation of ball-like agglomerates with an average diameter from 100 nm to 1500 nm (Fig. 5, right-top), being much bigger than from the sonochemical route (Fig. 1).

The BET surface area of ionothermally prepared $SrTiO_3$ ($18.22 \, m^2 \, g^{-1}$) is significantly lower than that of sonochemically prepared $SrTiO_3$ ($47.1 \, m^2 \, g^{-1}$) (Fig. SI-9). Due to the higher reaction temperature compared to the sonochemical reaction the ionic liquid does not longer act as structure-directing agent but only as solvent, thus less porosity is induced. Fig. 7 shows the catalytic activities of the ionothermal prepared $SrTiO_3$ compared to the sonochemical prepared sample. It can be seen that without co-catalyst the ionothermal prepared sample exhibits a higher activity than the sonochemical prepared sample. The reason is possibly related to the effect of the obtained by-phase anatase, forming nanocomposites with the $SrTiO_3$, which can reduce the recombination of charge carriers at the surface of ionothermal prepared sample. We have roughly calculated band positions of $SrTiO_3$ and
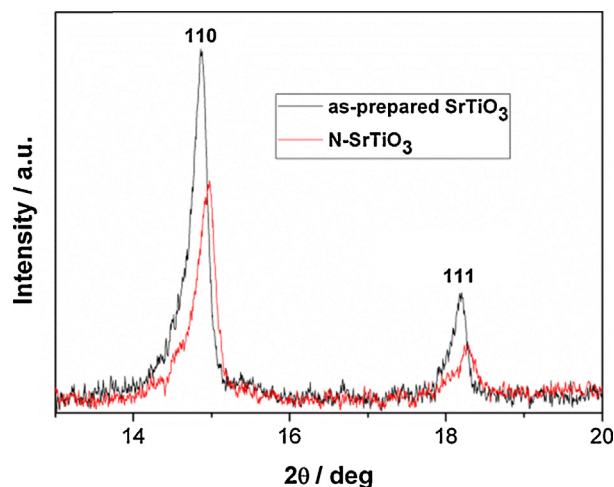
TiO_2 according to a simple procedure proposed by Butler and Ginley [10,42], where the estimated band gaps from UV–vis spectroscopy of the samples, the electronegativities and the ionization energies of the respective elements are used. A possible mechanism for charge transfer is shown in Fig. SI-10. The calculated conduction band of $SrTiO_3$ is located at a more negative potential (0.68 eV) compared to the conduction band of TiO_2 (0.29 eV). Thus, photoexcited electrons can be transferred from the conduction band of $SrTiO_3$ to anatase for charge separation, and the recombination probability with the valence band holes in $SrTiO_3$ is reduced. So with the procedure of Butler and Ginley a difference of ~390 mV could be calculated. According to the literature the conduction band of $SrTiO_3$ is 200 mV more negative than that of TiO_2 [43].

Photodeposition of 0.025 wt.% Rh, however, leads to an enhancement of H_2 evolution rates from 440 μmol/h to 800 μmol/h for the ionothermally prepared sample whereas for the sonochemically prepared sample an increase from 225 μmol/h to 1110 μmol/h was observed. The positive effect of the increased charge separation of the nanocomposite is noticeable for the activity without co-catalyst. However, in the presence of TiO_2 according to the calculated energy scheme in Fig. SI-9 the photoexcited electrons are transferred to the TiO_2. Thus the Rh is preferably deposited there, where it is less active than on the $SrTiO_3$. Thus, the activity increase of the sonochemically prepared sample is much higher due to the reduced recombination since Rh acts as the better electron sink.

Moreover, more Rh is needed for best activation in the ionothermally prepared sample, showing in addition that the smaller particle sizes in the sonochemically obtained samples are also advantageous.

3.5. Nitrogen-doped $SrTiO_3$

The XRD patterns of $SrTiO_3$ and N–$SrTiO_3$ in the region of the (1 1 0) and (1 1 1) reflexes are shown in Fig. 8. The diffraction peak positions for N-doped $SrTiO_3$ shifted to slightly higher angles indicating a shrinkage of the lattice constant of the cubic structure from 0.3895(12) nm to 0.373(3) nm for the N-containing material.

This decrease can be attributed to the formation of anion vacancy for charge compensation as $SrTiO_{3-3y/2}N_{y□y/2}$ (□: lattice defect) [44]. The average crystallite size of the N–$SrTiO_3$ estimated from the Scherrer equation amounts to 14.4 nm, which is almost the same as that of the as-synthesized $SrTiO_3$ (14.2 nm). EDX spectra and map images of N–$SrTiO_3$ (Fig. SI-11) confirm the presence and incorporation of nitrogen in the $SrTiO_3$ network. Fig. SI-12 shows the nitrogen adsorption–desorption isotherm of N–$SrTiO_3$, where
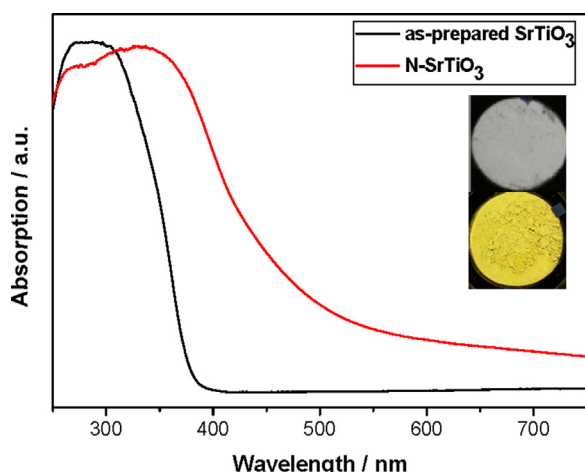
Fig. 9. UV–vis absorption spectra of sonochemically prepared SrTiO$_3$ and N–SrTiO$_3$.

the BET surface area of N-SrTiO$_3$ (10.1 m^2 g^{-1}) is significantly less than that of SrTiO$_3$ (47.1 m^2 g^{-1}). The quite strong decrease in surface area indicates a partial collapse of the small mesopores formed in the as-synthesized samples due to the presence to ionic liquid during the heat treatment at 450 °C.

Fig. 9 shows a comparison of the UV–vis absorption spectra of pure SrTiO$_3$ and N-SrTiO$_3$ demonstrating that the absorption edge of N-SrTiO$_3$ is shifted toward the visible region compared to that of SrTiO$_3$, where the absorption edges of SrTiO$_3$ and N-SrTiO$_3$ are observed at about 382 nm and 489 nm, corresponding to the band gaps of 3.1 eV and 2.1 eV (Fig. SI-13), respectively. The decrease of band gap of SrTiO$_3$ after doping with nitrogen can be understood in terms of the formation nitrogen centered energy states between the energy states of SrTiO$_3$, owing to replacement of oxide by nitride anions [45]. Visibly, the color of the samples turned from white for SrTiO$_3$ to yellow for N-SrTiO$_3$ as shown in the insert of Fig. 9. Thus, these results show that the incorporation of nitrogen into the lattice of SrTiO$_3$ leads to an alteration of the crystal and electronic properties of SrTiO$_3$.

Fig. 7 shows the photocatalytic activities of sonochemically prepared SrTiO$_3$ and N-SrTiO$_3$ for the hydrogen production under irradiation of UV light. Under the irradiation of UV light N-SrTiO$_3$ showed lower activity than SrTiO$_3$ due to the increase of the amount of lattice defects which act as the recombination centers for photogenerated electrons and holes. As expected, due to the large band gap for SrTiO$_3$ no activity can be detected under visible light irradiation, whereas the H$_2$ evolution rate of N-SrTiO$_3$ after photodeposition of Rh is about 25 ± 5 μmol/h. This value is well above the limit of our detection system which lies at about 10 μmol/h. Yu et el determined an activity of 1.2 μmol/h for 0.5wt.%Pt/N-doped SrTiO$_3$ in 18% MeOH/H$_2$O solution, synthesized via sol–gel hydrothermal method at 900 °C (300 W Xe lamp) [46]. Furthermore, the strontium titanate nanomaterials doped with nitrogen at a temperature range between 625 °C and 650 °C under ammonia gas atmosphere show photocatalytic performance between 0.2 and 41.3 μmol h^{-1} using methanol as a hole scavenger and Pt (0.5 wt.%) nanoparticles as a co-catalyst under visible light irradiation [47]. Taking into account the much lower preparation temperatures we used and the much smaller noble metal amounts we need, the sonochemical synthesis route described here demonstrates again its power.

4. Conclusions

We have successfully synthesized the titanates SrTiO$_3$ and BaTiO$_3$ as nanocrystals with cubic perovskite structure by a novel one-step ultrasound synthesis in the presence of an ionic liquid. This method is simple, reproducible, requires no for these two titanates additional thermal treatment and has no need for additional templates or surfactants, since the ionic liquid concurrently acts as solvent and template. However, the choice of the alkaline earth metal was found to be important since crystalline CaTiO$_3$ could in contrast only be obtained after subsequent calcination.

The photocatalytic experiments for H$_2$ evolution and for photodegradation of methylene blue reveal that the MTiO$_3$ (Ca, Sr, Ba) show different catalytic activity. The highest photocatalytic activity for H$_2$ evolution is with about 1.1 mmol/h obtained for SrTiO$_3$ using only very little (0.025 wt.%) photodeposited Rh as co-catalyst. It was found that subsequent heating of the sonochemically prepared SrTiO$_3$ has a negative effect on the surface area and results in lower photocatalytic activity. Ionothermally obtained TiO$_2$–SrTiO$_3$ exhibits without co-catalyst a higher activity than the sonochemically prepared neat SrTiO$_3$ due to the synergistic effect of anatase on the electronic structure of SrTiO$_3$, but this synergy is overcompensated after photodepostirion of Rh showing that the photoelectrons are preferentially migrate to the Rh. Nitrogen-doped SrTiO$_3$ showed photocatalytic acivity under visible light irradiation due to the formation of new states in the band gap allowing absorption of visible light.

Appendix A. Supplementary data

Supplementary material related to this article can be found, in the online version, at http://dx.doi.org/10.1016/j.apcatb.2014.11.010.

References

[1] K. Maeda, K. Domen, J. Phys. Chem. Lett. 1 (2010) 2655–2661.
[2] F.E. Osterloh, Chem. Soc. Rev. 42 (2013) 2294–2320.
[3] N. Wang, D. Kong, H. He, Powder. Technol. 207 (2011) 470–473.
[4] A. Gedanken, Ultrason. Sonochem. 11 (2004) 47–55.
[5] D.J. Flannigan, S.D. Hopkins, K.S. Suslick, J. Organomet. Chem. 690 (2005) 3513–3517.
[6] S. Manickam, in: M. Pankaj, Ashokkumar (Eds.), Theoretical and Experimental Sonochemistry Involving Inorganic Systems, Springer, Heidelberg, 2011, pp. 191–192.
[7] Y. Chauvin, H. Olivier-Bourbigou, Chem. Tech. 25 (1995) 26–30.
[8] T. Gutel, C.C. Santini, K. Philippot, A. Padua, K. Pelzer, B. Chaudret, Y. Chauvin, J.-M. Basset, J. Mater. Chem. 19 (2009) 3624–3631.
[9] P. Webb, M. Sellin, T. Kunene, S. Williamson, A. Slawin, D. Cole-Hamilton, J. Am. Chem. Soc. 125 (2003) 15577–15588.
[10] R. Marschall, J. Soldat, M. Wark, Photochem. Photobiol. Sci. 12 (2013) 671–677.
[11] K. Maeda, K. Domen, J. Phys. Chem. C 111 (2007) 851–7861.
[12] H. Weingärtner, Angew. Chem. Int. Ed. 47 (2008) 654–670.
[13] K. Noack, P.S. Schulz, N. Paape, J. Kiefer, P. Wasserscheid, A. Leipertz, Phys. Chem. Chem. Phys. 12 (2010) 14153–14161.
[14] J.F. Brennecke, R.D. Roger, K.R. Seddon, Ionic Liquids IV, Oxford University Press, 2007, pp. 12.
[15] K.J. Klabunde, R.M. Richards, Nanoscale Materials in Chemistry, John Wiley & Sons, Inc, 2009, pp. 78.
[16] A.F. Wells, Structural Inorganic Chemistry, Oxford University Press, 1991, pp. 585.
[17] N.L. Ross, R.J. Angel, Am. Miner. 84 (1999) 277–281.

[18] F. Bai, H. Zheng, H. Cao, L.E. Cross, R. Ramesh, J. Li, D. Viehland, Appl. Phys. Lett. 85 (2004) 4109–4111.
[19] L.S. Cavalcante, V.S. Marques, J.C. Sczancoski, M.T.E. Scote, M.R. Joya, J.A. Varela, M.R.M.C. Santos, Chem. Eng. J. 143 (2008) 299–307.
[20] Y.I. Yuzyuk, Phys. Solid State 54 (2012) 1026–1059.
[21] L.F. Dasilva, W. Avansi Jr., J. Andres, C. Riberio, M.L. Moreira, E. Longo, V.R. Mastelaro, Phys. Chem. Chem. Phys. 15 (2013) 12386–12393.
[22] A.E. Souza, G.T.A. Santos, B.C. Barra, W.D. Macedo, S.R. Teixeira, C.M. Santos, A.M.O.R. Senos, L. Amaral, E. Longo, Cryst. Growth Des. 12 (2012) 5671–5679.
[23] W.G. Spitzer, R.C. Miller, D.A. Kleinman, L.E. Howarth, Phys. Rev. 126 (1962) 1710–1721.
[24] J. Tauc, Mater. Res. Bull. 3 (1968) 37–41.
[25] W. Zhang, F. Bi, X. Sun, H. He, Asian J. Chem. 25 (2013) 5311–5315.
[26] T. Puangpetch, T. Sreethawong, S. Yoshikawa, S. Chavadej, J. Mol. Catal. A: Chem. 287 (2008) 70–79.
[27] L.F. da Silva, L.J.Q. Maia, M.I.B. Bernardi, J.A. Andrés, V.R. Mastelaro, Mater. Chem. Phys. 125 (2011) 168–173.
[28] W. Lu, M. Quilitz, H. Schmidt, J. Eur. Ceram. Soc. 27 (2007) 3149–3159.
[29] S.S. Gaikwad, A.V. Borhade, V.B. Guikwad, Der Pharma Chem. 4 (2012) 184–193.
[30] H. Donga, G. Chen, J. Sun, C. Li, Y. Yu, D. Chen, Appl. Catal. B 134 (2013) 46–54.
[31] T. Xian, H. Yang, Adv. Mater. Res. 418–420 (2012) 18–21.
[32] H. Zhao, Y. Duan, X. Sun, New J. Chem. 37 (2013) 986–991.
[33] X. Lin, J. Xing, W. Wang, Z. Shan, F. Xu, F. Huang, J. Phys. Chem. C. 111 (2007) 18288–18293.
[34] A.A. Ismail, D.W. Bahnemann, L. Robben, V. Yarovyi, M. Wark, Chem. Mater. 22 (2010) 108–116.
[35] D. Sukkim, S.-Y. Kwak, Environ. Sci. Technol. 43 (2009) 148–151.
[36] A. Kudo, Y. Miseki, Chem. Soc. Rev. 38 (2009) 253–278.
[37] D.-N. Bui, J. Mu, L. Wang, S.-Z. Kang, Y. Li, Appl. Surf. Sci. 274 (2013) 328–333.
[38] T. Puangpetch, T. Sreethawong, S. Yoshikawa, S. Chavadej, J. Mol. Catal. A: Chem. 312 (2009) 97–106.
[39] E.R. Cooper, C.D. Andrews, P.S. Wheatley, P.B. Webb, P. Wormald, R.E. Morris, Nature 430 (2004) 1012–1016.
[40] D. Chen, S.K. Sharma, A. Mudhoo, Handbook on Applications of Ultrasound Sonochemistry for Sustainability, CRC Press, Inc, 2012, pp. 560.
[41] W. Wang, S. Liang, K. Ding, J. Bi, J.C. Yu, P.K. Wang, L. Wu, J. Mater. Sci. 49 (2014) 1893–1902.
[42] M.A. Butler, D.S. Ginley, J. Electrochem. Soc. 125 (1978) 228–232.
[43] Z. Jiao, T. Chen, J. Xiong, T. Wang, G. Lu, J. Ye, Y. Bi, Sci. Rep. 3 (2720) (2013) 1–6.
[44] U. Sulaeman, S. Yin, T. Sato, J. Nanomater. (2010) 6, 629727.
[45] T.S. Le, Q.B. Ngo, V.D. Nguyen, T.H. Dao, X.T. Tran, E.N. Kabachkov, I.L. Balkihin, Adv. Nat. Sci.: Nanosci. Nanotechnol. 5 (2014) 015017, 6 pp.
[46] H. Yu, S. Yan, Z. Li, T. Yu, Z. Zou, Int. J. Hydrog. Energy 37 (2012) 12120–12127.
[47] N. Nuraje, Y. Lei, A. Belcher, Catal. Commun. 44 (2014) 68–72.